Net precipitation of Antarctica: thermodynamical and dynamical parts of the climate change signal

Grieger, Jens; Leckebusch, Gregor C.; Ulbrich, Uwe

DOI:
10.1175/JCLI-D-14-00787.1
10.1175/JCLI-D-14-00787.1

Net Precipitation of Antarctica: Thermodynamical and Dynamical Parts of the Climate Change Signal

JENS GRIEGER

Institute of Meteorology, Freie Universität Berlin, Berlin, Germany

GREGOR C. LECKEBUSCH

School of Geography, Earth and Environmental Sciences, University of Birmingham, Birmingham, United Kingdom

UWE ULBRICH

Institute of Meteorology, Freie Universität Berlin, Berlin, Germany

(Manuscript received 18 November 2014, in final form 24 June 2015)

ABSTRACT

This paper investigates climate change signals of Southern Hemisphere (SH) moisture flux simulated by three members of one CMIP3 coupled atmosphere–ocean general circulation model (AOGCM) and a multimodel ensemble of CMIP5 simulations. Generally, flux changes are dominated by increased atmospheric moisture due to temperature increase in the future climate projections. An approach is presented to distinguish between thermodynamical and dynamical influences on moisture flux. Furthermore, a physical interpretation of the transport changes due to dynamics is investigated by decomposing atmospheric waves into different length scales and temporal variations. Signals of moisture flux are compared with fluctuations of geopotential height fields as well as climate signals of extratropical cyclones. Moisture flux variability in the synoptic length scale with temporal variations shorter than 8 days can be assigned to the SH storm track. Climate change signals of these atmospheric waves show a distinctive poleward shift. This can be attributed to the climate change signal of extratropical cyclones. Furthermore, the climate change signal of atmospheric waves can be better understood if strong cyclones that intensify especially on the Eastern Hemisphere are taken into account. Antarctic net precipitation is calculated by means of the vertically integrated moisture flux. Future projections show increasing signals of net precipitation, whereas the dynamical part of net precipitation decreases. This can be understood by means of the low-variability component of synoptic-scale waves, which show a decreasing signal, especially off the coast of West Antarctica. This is shown to be due to changing variability of the Amundsen–Bellingshausen Seas low.

1. Introduction

The general energy deficit of the polar regions is compensated by poleward energy fluxes, such as atmospheric transports of latent and sensible heat (Peixoto and Oort 1992). Southern Hemisphere (SH) poleward atmospheric fluxes have major impacts on the Antarctic climate (i.e., temperature and moisture accumulation) (e.g., Yamazaki 1992; Turner et al. 1995; Connolley and King 1993; Bromwich et al. 1995; Cullather et al. 1998). In particular, the transient component of moisture flux is the dominating part over the SH midlatitudes (Peixoto and Oort 1983). The amount of moisture that is transported toward Antarctica is an important part of the atmospheric contribution to Antarctic surface mass balance (SMB). Estimation of SMB can be done by in situ observations, remote sensing, and atmospheric modeling, where each technique has to deal with its own difficulties regarding the extreme weather conditions of Antarctica (Turner et al. 2009, and references therein). Previous studies have analyzed the precipitation and evaporation of Antarctica by means of climate models and reanalysis products, respectively (Bromwich et al. 2004; Monaghan et al. 2006; Tietvinen and Vihma 2008). Differences of results depend on the different datasets and methods as well as varying time periods for the analysis (Tietvinen and Vihma 2008).

Corresponding author address: Jens Grieger, Institute of Meteorology, Freie Universität Berlin, Carl-Heinrich-Becker-Weg 6-10, 12165 Berlin, Germany.
E-mail: jens.grieger@met.fu-berlin.de

DOI: 10.1175/JCLI-D-14-00787.1

Understanding processes of the SMB variations of Antarctica in recent and future climate is an important issue since the Antarctic ice sheet could provide an enormous potential contribution to sea level rise. According to both phase 3 and phase 5 of the Coupled Model Intercomparison Project (CMIP3 and CMIP5) future projections of global climate models, Antarctica is likely to be a negative contributor to sea level rise in the twenty-first century (Meehl et al. 2007a; Church et al. 2013).

Uotila et al. (2007) investigated Antarctic net precipitation [i.e., precipitation minus evaporation ($P - E$)] by means of an ensemble of CMIP3 coupled atmosphere–ocean general circulation models (AOGCMs). With respect to the climate change signal at the end of the twenty-first century, they found an increase for almost all models. Using the approach of the identification of circulation weather types, they distinguished between thermodynamical and dynamical effects. Uotila et al. (2007) concluded that thermodynamics dominate the climate change signal and that the dynamical part has a small impact on the increase, especially for the whole of Antarctica.

Held and Soden (2006) analyzed the climate change of the hydrological cycle simulated by an ensemble of CMIP3 AOGCMs and discussed changing net precipitation to be a function of changes of global near-surface temperature. They found a robust intensification of the hydrological cycle due to global warming simulated by their analyzed multimodel ensemble. Seager et al. (2010) analyzed different components of moisture transport. They split the mean meridional flux into thermodynamical and dynamical parts but remarked that this is not straightforward for the transient component of transport since it is a covariance. Lorenz and DeWeaver (2007) discussed changes in the hydrological cycle to be a function of zonal mean temperature at 850 hPa. In comparison to Held and Soden (2006), this is a more local response of humidity change to temperature variations. The relationship between temperature increase and Antarctic ice accumulation is shown to be robust for the analysis of ice core data, paleo simulations, and future climate projections with recent GCMs (Frieler et al. 2015).

Our study aims to investigate to what extent it is possible to explain the future increase of Antarctic net precipitation only by increasing amounts of atmospheric humidity. The residuum of the climate change signal that cannot be understood by changes of atmospheric moisture content is attributed to changes of the atmospheric circulation. Therefore, atmospheric waves of moisture transport are decomposed into different length scales and temporal variations. These are compared with fluctuations of geopotential height fields as well as climate signals of extratropical cyclones.

In section 2, we describe the analyzed climate model and reanalysis data as well as the methodology used for the flux investigation and the objective algorithm for cyclone identification. The validation of model precipitation with reanalysis and the evaluation of SH moisture transport is done in section 3. Here, we also include a discussion of the climate change signals of moisture flux and geopotential height variations, with respect to their different decompositions, as well as cyclone activity. At the end of this section, the change of net precipitation within the Antarctic Circle is addressed. Finally, in section 4, we present the conclusions of our findings.

2. Data and methods

a. *Coupled atmosphere–ocean general circulation model and reanalysis*

Major analysis is done with three members of one AOGCM that has been evaluated within CMIP3 (Meehl et al. 2007b). The AOGCM consists of the atmospheric component ECHAM5 (Roeckner et al. 2003), computed at a horizontal resolution that is triangular truncated at wavenumber 63 (T63), and the oceanic model MPI-OM (Marsland et al. 2003). Parts of the study have also been done with a more recent ensemble of climate models that have been analyzed within CMIP5 (Taylor et al. 2012). The model setting for our investigation is chosen in this way because of data availability. For a good representation of vertically integrated moisture transport as well as the possibility to distinguish between mean and transient flux components, the CMIP3 standard data availability for three-dimensional daily variables, which consists of 9 pressure levels between 1000 and 200 hPa, is considered to be insufficient (Uotila et al. 2007). Furthermore, CMIP5 model output standards are also inadequate. In the analysis of this current study, 6-hourly data on 11 pressure levels between 1000 and 200 hPa (1000, 925, 850, 775, 700, 600, 500, 400, 300, 250, and 200) have been used. This data availability could be achieved for the ECHAM5 model run.

Additionally, one simulation of eight CMIP5 models is used (Table 1) to evaluate moisture flux for one single pressure level (850 hPa) using daily mean data.

Validation is performed with the 40-yr European Centre for Medium-Range Weather Forecasts (ECMWF) Re-Analysis (ERA-40) data (Uppala et al. 2005). SH reanalysis has to deal with sparse observational data, especially in the presatellite era. ERA-40 is shown to perform well since satellite products have been used for the reanalysis from the late 1970s (Bromwich and Fogt 2004). Therefore, 20 years of ERA-40 data (1981–2000) are used in this study on a horizontal resolution of 2.5° × 2.5°, which seems to be a fairer comparison with AOGCM data, especially for the identification of

TABLE 1. CMIP5 models used in this study.

Modeling center	Model name
Canadian Centre for Climate Modelling and Analysis	CanESM2
Centro Euro-Mediterraneo per I Cambiamenti Climatici	CMCC-CM
Commonwealth Scientific and Industrial Research Organization in collaboration with Queensland Climate Change Centre of Excellence	CSIRO Mk3.6.0
LASG, Institute of Atmospheric Physics, Chinese Academy of Sciences and Center for Earth System Science (CESS), Tsinghua University	FGOALS-g2
L'Institut Pierre-Simon Laplace	IPSL-CM5A-LR
Atmosphere and Ocean Research Institute, University of Tokyo National Institute for Environmental Studies, and Japan Agency for Marine-Earth Science and Technology	MIROC5
Max Planck Institute for Meteorology	MPI-ESM-LR
Meteorological Research Institute	MRI-CGCM3

extratropical cyclones (Grieger et al. 2014). The three AOGCM members have also been analyzed between 1981–2000 and 2081–2100 following the SRES A1B scenario (Nakicenovic et al. 2000). In principle, the whole investigation has been done for the extended austral winter season (i.e., April–September). Primary analysis of precipitation as well as the discussion of annual cycles has been done for the whole year. Finally, results are compared to those for the austral summer season (October–March), and this is discussed in section 4.

For the calculation of atmospheric moisture flux, 3D data of horizontal wind and specific humidity have been analyzed. Method validation of calculated net precipitation by means of moisture flux convergence is done by an evaluation of direct AOGCM output of large-scale and convective precipitation and evaporation. The storm track is investigated by means of the 500-hPa geopotential height. Finally, the objective algorithm for the identification and tracking of extratropical cyclones uses mean sea level pressure (MSLP) as the input.

In the following, for the horizontal geographical plots, the mean of the three ensemble members is shown as results of the twentieth century and climate change signals. Statistical significance is calculated out of the mean and interannual variance of 60 years of the three members (3×20 yr). Figures of the flux convergence over Antarctica show each member separately.

b. *Hydrological cycle, moisture flux, and flux divergence*

Net precipitation can be computed by means of the evaluation of the hydrological cycle (e.g., Bromwich et al. 1995; Cullather et al. 1998). We begin with the vertically integrated moisture flux vector $\mathbf{Q}$ [Eq. (1)]. Generally, moisture flux is defined to be positive in the northward direction. This study deals with SH moisture transport and its relevance for Antarctica (i.e., poleward moisture flux is an important quantity here). Hence, throughout the paper, southward moisture flux is defined to be positive to make it easier to interpret climate change signals of poleward moisture transport.

$$\mathbf{Q} = \frac{1}{g}\int_{p_{\mathrm{sfc}}}^{p_0} q_{(p)}\mathbf{v}_{(p)}\,dp, \tag{1}$$

where g is acceleration of gravity, q is specific humidity, and $\mathbf{v}$ is the horizontal wind vector. Moisture flux is integrated from surface pressure p_{sfc} to $p_0 = 200$ hPa. The divergence of $\mathbf{Q}$ can be written as

$$\langle E - P\rangle = \langle \nabla \mathbf{Q}\rangle + \left\langle \frac{\partial W}{\partial t}\right\rangle, \tag{2}$$

where $\langle . \rangle$ denotes areal averaging and W is total column water vapor (TCWV). The temporal mean $\overline{(.)}$ of Eq. (2) can be written as

$$\overline{\langle E - P\rangle} = \overline{\langle \nabla \mathbf{Q}\rangle}, \tag{3}$$

since $\overline{\langle \partial W/\partial t\rangle}$ is small for seasonal and longer time scales (Bromwich 1988).

Equation (3) can be written as a line integral using Gauss's theorem (Bromwich and Robasky 1993). This simplifies the calculation of net precipitation south of an arbitrary polar cap for gridded datasets, since the zonal component u of wind vector $\mathbf{v}$ is no longer needed for the evaluation.

$$\overline{\langle E - P\rangle} = \frac{1}{A}\frac{1}{g}\oint\left\{\int_{p_{\mathrm{sfc}}}^{p_0} q_{(p)}v_{(p)}\,dp\right\}dl, \tag{4}$$

where A is the area of the polar cap, and dl is the increment on the line around the cap.

c. *Reynolds decomposition*

Reynolds decomposition can be performed to distinguish between mean and eddy flux components. Any quantity A can be separated into its average $\overline{A}$ and a perturbation A':

$$A(t) = \overline{A} + A'(t). \tag{5}$$

Using Eq. (5) for moisture flux Q, which is the product of specific humidity q and horizontal wind v, the decomposition can be written as follows:

$$\overline{Q} = \frac{1}{g}\int dp\ \overline{qv} = \underbrace{\frac{1}{g}\int dp\ \overline{q}\,\overline{v}}_{\text{MME}} + \underbrace{\frac{1}{g}\int dp\ \overline{q'v'}}_{\text{TE}}, \tag{6}$$

where the first part is the transport due to the mean meridional circulation (MMC), and the second part is the component of transient eddies (TE). In the SH extratropics, the most important part of meridional transport is due to transient flux perturbations (Peixoto and Oort 1983), which are also highly relevant for the Antarctic region (Bromwich et al. 1995; Cullather et al. 1998).

This decomposition is done for each winter season (April–September) separately to allow for the possibility of analyzing interannual variability.

d. Wave decomposition

For an assignment of atmospheric wave components to different physical mechanisms, we follow the approach of Blackmon (1976), who investigated 500-hPa geopotential height fields for the Northern Hemisphere (NH). Blackmon (1976) used spectral truncation to decompose geopotential height variability into three length scales. Furthermore, he used a bandpass filter to distinguish between three different time scales. In particular the time scale between 2.5 and 6 days is typically known as the storm track. Wu et al. (2011) investigated geopotential height variances as well as atmospheric energy fluxes with a bandpass filter between 2 and 8 days to analyze the synoptic scale.

In our study, we want to decompose transient moisture flux ($q'v'$) and geopotential height anomalies ($z'z'$) into two different length- and time-scale variations. Therefore, we use only one spectral truncation and one low-pass filter and calculate the residuals to obtain the corresponding components. For the long-wave scale, wavenumbers greater than 7 are truncated, and the residual of the field is used as the synoptic scale. A 21-point low-pass filter is used to define low-frequency fluctuations longer than 8 days. Again, the corresponding (high frequency) component of $q'v'$ and $z'z'$ is calculated by means of the residual. For the vertically integrated moisture flux, spatial and temporal filters are performed at each pressure level separately prior to the vertical integration.

Referring to Blackmon (1976), the SH storm track is defined as the synoptic-scale, high-frequency fluctuations of the 500-hPa geopotential height anomaly. Straightforwardly, the transient component of the vertically integrated meridional moisture flux is divided into long transient and synoptic waves of both low- and high-frequency fluctuations. In the following, the synoptic scale is especially discussed since this component dominates poleward atmospheric moisture transport.

e. Splitting thermodynamical and dynamical parts of moisture flux

If the climate change signal of moisture flux is investigated, it is often considered to be mainly influenced by atmospheric temperature increase since the hydrological cycle is strengthened in a warmer climate (e.g., Held and Soden 2006; Lorenz and DeWeaver 2007). Nevertheless, atmospheric circulation is changing in the future projections, both generally and for regions that are important for atmospheric poleward moisture transport (i.e., the tropospheric midlatitudes) (e.g., Bengtsson et al. 2006; Grieger et al. 2014). Therefore, it is meaningful to perform an investigation of both thermodynamical and dynamical parts of the climate change signal of moisture transport and to distinguish between these parts.

Using Eq. (6), the climate change signal of the meridional moisture flux $\delta\overline{Q}$ is decomposed into the change of MMC and TE:

$$\delta Q = \delta\mathrm{MMC} + \delta\mathrm{TE}, \tag{7}$$

whereas the climate change signal of MMC can be analytically split into thermodynamical and dynamical parts (Seager et al. 2010):

$$\delta\mathrm{MMC} = \delta\mathrm{MMC}_{\mathrm{th}} + \delta\mathrm{MMC}_{\mathrm{dyn}} + \delta\mathrm{MMC}_{\mathrm{nl}} \tag{8}$$

$$= (\delta\overline{q})\overline{v}_{20\mathrm{C}} + \overline{q}_{20\mathrm{C}}(\delta\overline{v}) + (\delta\overline{q})(\delta\overline{v}). \tag{9}$$

In the mid and high latitudes, MMC has little influence on total moisture transport. Therefore, it is preferred to also decompose TE by means of a scaling approach motivated by previous studies. We start with the result that climate changes of net precipitation can be written as a function of projected temperature changes, assuming that the general circulation is unchanged (Held and Soden 2006; Lorenz and DeWeaver 2007). Held and Soden (2006) evaluate net precipitation as a function of global near-surface temperature, whereas Lorenz and DeWeaver (2007) used the approach of analyzing the hydrological cycle as a function of zonal mean temperature at 850 hPa. Since we investigate moisture flux in the SH mid and high latitudes, it is meaningful to follow the approach of Lorenz and DeWeaver (2007), which takes into account local differences of temperature and moisture change. Assuming constant relative humidity in the future projection,

specific humidity q increases at an exponential Clausius–Clapeyron rate (Held and Soden 2006):

$$\frac{q_{\mathrm{A1B}}}{q_{\mathrm{20C}}} = \exp[\alpha(T_{\mathrm{A1B}} - T_{\mathrm{20C}})]. \tag{10}$$

Lorenz and DeWeaver (2007) considered the relationship of Eq. (10) to be valid also for TCVW W as well as moisture flux Q, assuming no changes in the atmospheric circulation. Thus, the relation of Eq. (10) can also be used to describe the quotient of the thermodynamically influenced moisture fluxes as well that as for its transient component TE:

$$\left(\frac{\mathrm{TE}_{\mathrm{A1B}}}{\mathrm{TE}_{\mathrm{20C}}}\right)_{\mathrm{th}} = \left(\frac{Q_{\mathrm{A1B}}}{Q_{\mathrm{20C}}}\right)_{\mathrm{th}} = \frac{W_{\mathrm{A1B}}}{W_{\mathrm{20C}}} = \exp[\alpha(T_{\mathrm{A1B}} - T_{\mathrm{20C}})]. \tag{11}$$

The relation of moisture flux in Eq. (11) is only valid for the assumption of an unchanged atmospheric circulation. The projected moisture flux $\mathrm{TE}_{\mathrm{A1B}}$ is influenced by both an increase of TCWV and circulation changes. We use Eq. (11) to compute a scaled flux $\widehat{\mathrm{TE}}_{\mathrm{A1B}}$ for the future projection:

$$\widehat{\mathrm{TE}}_{\mathrm{A1B}} = \mathrm{TE}_{\mathrm{A1B}} \frac{W_{\mathrm{20C}}}{W_{\mathrm{A1B}}}, \tag{12}$$

where $W = W(\phi)$ is the zonal mean of TCWV. The fluxes $\widehat{\mathrm{TE}}_{\mathrm{A1B}}$ and $\mathrm{TE}_{\mathrm{A1B}}$ differ in the mean moisture content, whereas $\widehat{\mathrm{TE}}_{\mathrm{A1B}}$ and $\mathrm{TE}_{\mathrm{20C}}$ differ in the circulation. The climate change signal of the transient moisture flux $\delta\mathrm{TE}$ is decomposed by the scaled flux of Eq. (12):

$$\delta\mathrm{TE} = \mathrm{TE}_{\mathrm{A1B}} - \mathrm{TE}_{\mathrm{20C}} \tag{13}$$

$$= \underbrace{\mathrm{TE}_{\mathrm{A1B}} - \widehat{\mathrm{TE}}_{\mathrm{A1B}}}_{\delta\mathrm{TE}_{\mathrm{th}}} + \underbrace{\widehat{\mathrm{TE}}_{\mathrm{A1B}} - \mathrm{TE}_{\mathrm{20C}}}_{\delta\mathrm{TE}_{\mathrm{dyn}}} \tag{14}$$

In the following, we mainly discuss the dynamical part of the climate signal $\delta\mathrm{TE}_{\mathrm{dyn}}$.

f. Objective cyclone tracking algorithm

For the comparison of the storm track with statistics of extratropical cyclones, we use an objective algorithm for cyclone identification and tracking developed by Murray and Simmonds (1991), with modification specified by Simmonds and Murray (1999) and Simmonds et al. (1999). Only a short description of the algorithm is given here. The methodology uses 6-hourly values of MSLP as input data. The MSLP field is interpolated with a bicubic spline function to a polar stereographic grid. Regions above 1000 m are generally not used because of the necessary interpolation of pressure values to sea level. The algorithm looks for maxima of the Laplacian of MSLP on the new stereographic grid. Local minima of the MSLP are assigned to these maxima of the Laplacian and define cyclone cores. If there is no minimum within a radius of 6° latitude, the pressure inflection point is used to define an open cyclonic system. The tracking of the identified cyclone centers is done by a prediction of subsequent cyclone positions in the next time step. Finally, the predicted and identified cyclone positions are compared in order to connect the identified centers, thus forming cyclone tracks. A more detailed description of the settings can be found in Grieger et al. (2014).

3. Results

a. Reanalysis and AOGCM 20C

1) Precipitation and net precipitation

At first, precipitation (P) and net precipitation ($P - E$), respectively, will be investigated for ERA-40 and the ECHAM5 AOGCM integration. Therefore, reanalysis and AOGCM model output of precipitation and evaporation is analyzed on the same 2.5° × 2.5° horizontal grid as used for ERA-40 in this study (i.e., P and E are regridded by a conservative remapping).

SH precipitation patterns of ERA-40 show a distinctive gradient of high precipitation values over the Southern Ocean toward lower values over Antarctica (Fig. 1a). This general behavior is already discussed in previous studies (e.g., Bromwich 1988; Tietvinen and Vihma 2008). The regions at the coastline of the Amundsen and Bellingshausen Seas show maximum values of precipitation off the coast of Antarctica. For net precipitation, positive values (i.e., precipitation predominates evaporation) can be found at nearly every location between 50° and 90°S (Fig. 1b) except for downstream of the southern tip of South America and south of the Ross Sea. There are significant maximum values, which have already been found for precipitation at the Antarctic coastline of the Amundsen–Bellingshausen Seas and west of the Antarctic Peninsula.

General behavior of precipitation and net precipitation can be simulated by the investigated AOGCM runs (Figs. 1c,d), although differences are found in some details. The amount of precipitation over the Southern Ocean is generally higher in the AOGCM, whereas precipitation and net precipitation are underestimated west of the Antarctic Peninsula, which is likely because of the smoother topography of the AOGCM (cf. Bromwich et al. 2004). The lower orography of the Antarctic Peninsula also leads to a less pronounced

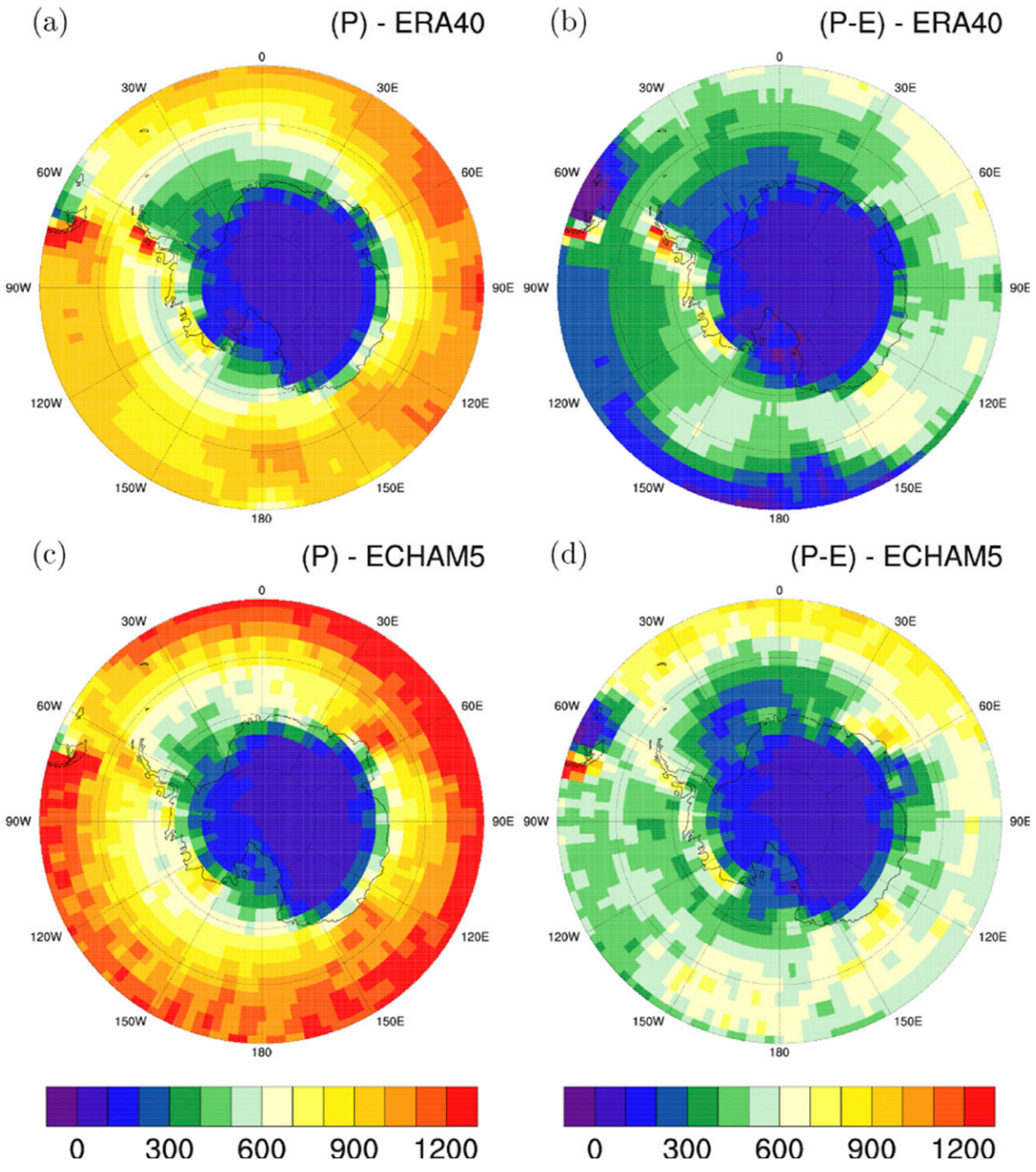

FIG. 1. Annual precipitation (mm yr^{-1}) for (a) ERA-40 and (c) ECHAM5 (ensemble of three runs); net precipitation ($P - E$) for (b) ERA-40 and (d) ECHAM5 (ensemble of three runs) between 1981–2000. Both ERA-40 and ECHAM5 have been regridded to the same 2.5° × 2.5° grid.

minimum in the Weddell Sea, which is caused by blocking of moist air (cf. Tietvinen and Vihma 2008). On the other hand, there are additional significant locations of high net precipitation off the coast of the Antarctic continent: namely, north of Enderby Land and north of Adelie Land (Fig. 1d). Although modeled P and E seem to have a bit more noise in comparison to ERA-40, the AOGCM generally simulates patterns for precipitation

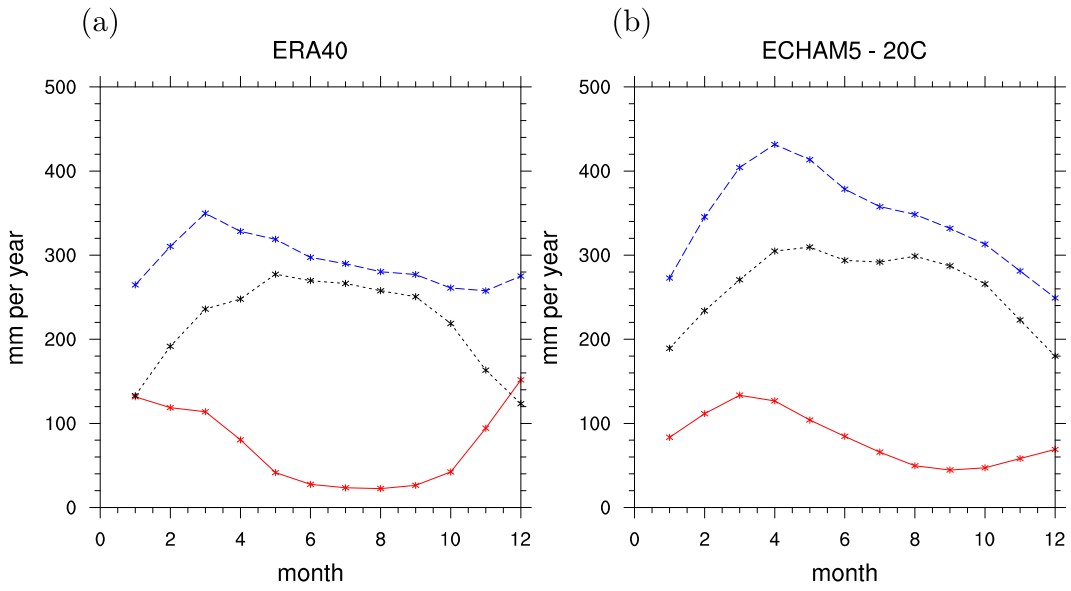

FIG. 2. Monthly climatology of precipitation (dashed blue), evaporation (solid red), and net precipitation (dotted black) for (a) ERA-40 and (b) ECHAM5 (ensemble of three runs) between 1981 and 2000 south of 67.5°S.

and net precipitation that compare well with the reanalysis. This is not obvious for a GCM integrated at T63 (cf. Genthon and Krinner 2001).

2) PRECIPITATION SOUTH OF 67.5°S

The reanalysis and the AOGCM analyzed in this study use different land–sea masks (LSM) as well as a different orography, which complicates a fair comparison of precipitation, since it is largely influenced by the representation of the Antarctic continent. Therefore, the region of interest is restricted to the spherical cap south of 67.5°S. By this choice, additional regridding is not necessary. To ensure that the new area is an acceptable representation of Antarctica in terms of net precipitation, the correlation between the $E - P$ (given as model output) of both areas is calculated. For monthly values of the analyzed period (1981–2000), correlations for the three members of the AOGCM are 0.88, 0.87, and 0.87, respectively.

Figure 2 shows the annual cycle for precipitation, evaporation, and the difference of these (i.e., net precipitation) south of 67.5°S for (Fig. 2a) ERA-40 and (Fig. 2b) ECHAM5. Precipitation peaks in March for ERA-40, with slightly decreasing values for the following months with respect to the annual cycle. Maximum values for evaporation can be found for austral summer (December–February), whereas it is almost zero in winter (June–August). Combination of both leads to an annual cycle of net precipitation, which is maximal for the extended winter season (April–September).

This general behavior can be found in previous studies (Bromwich et al. 1995; Cullather et al. 1998). The annual cycle simulated by ECHAM5 is shifted toward the winter season (i.e., maximum values of evaporation can be found in March and April), and precipitation peaks in April (Fig. 2b). As expected by the general characteristic of a higher amount of SH precipitation, simulated net precipitation over Antarctica is generally higher (Fig. 2) in comparison to ERA-40 (Fig. 1). Nevertheless, the annual cycle of net precipitation shows its maximum throughout the extended winter season, as found for ERA-40.

3) COMPARISON BETWEEN NET PRECIPITATION AND FLUX DIVERGENCE

Following Eq. (4), the divergence inside a spherical cap is calculated by moisture flux through the boundary (i.e., latitude of 67.5°S). Using the regridded data on the same 2.5° × 2.5° grid, $P - E$ and moisture flux convergence can easily be compared for the same region. Table 2 shows this comparison between net precipitation and flux convergence for ERA-40 and ECHAM5 from 1981 to 2000 for the

TABLE 2. Net precipitation and flux divergence for ERA-40 and the three runs of ECHAM5 south of 67.5°S from 1981 to 2000 for the whole year.

	$P - E$ (mm yr^{-1})	$-\overline{\langle \nabla Q \rangle}$ (mm yr^{-1})
ERA-40	219.6	215.2
Run 1	264.0	228.9
Run 2	258.2	223.6
Run 3	264.9	229.6

whole year. The results for ERA-40 match very well, possibly even better than in the study of Tietvinen and Vihma (2008). Perhaps this is because of the coarser grid used for our calculation leading to a smoother representation of the values, which can be beneficial for precipitation. The differences are higher for ECHAM5 (i.e., $P - E$ is about 15% higher than flux convergence), and this is consistent for each run. Therefore, it seems more to be a systematic bias than a general discrepancy. It is possible that the temporal and vertical resolution is still insufficient for a correct calculation of moisture flux convergence (Uotila et al. 2007). On the other hand, $E - P$ values have to be carefully discussed since it is known that climate models have difficulties in their representation of Antarctic precipitation (Genthon and Krinner 2001). Generally, it is assumed that the approach of moisture flux convergence can lead to more realistic results for certain regions if vertical and temporal resolution is sufficiently high.

Splitting moisture flux into components of MMC and TE by means of Eq. (6) results in a dominating role of TE for SH moisture flux in the mid and high latitudes, as shown by previous studies (e.g., Peixoto and Oort 1983; Bromwich et al. 1995; Cullather et al. 1998). At the latitude belts covering the Antarctic ice shield, MMC turns into an equatorward direction. This is because of katabatic winds, which play a dominant role for the near-surface wind system of Antarctica and are known to show high directional constancy (Tietvinen and Vihma 2008). In the current work, further investigation of moisture flux is done for the transient component, since this study focuses on the understanding of transport mechanisms from mid and high latitudes toward the Antarctic continent. Our discussion concentrates on the extended winter season (April–September) since $P - E$ shows maximum values for these months (Fig. 2). Figures 3a and 3b show the transient component of vertically integrated meridional moisture flux for ERA-40 and the AOGCM runs. The values are positive everywhere, which implies a poleward transport in the SH. As shown by previous studies (e.g., Peixoto and Oort 1983), maximum flux can be identified around 40°S downstream of the continents in the Atlantic, Indian, and Pacific Oceans. In comparison to ERA-40, it can be stated that the TE component of moisture flux is well characterized by ECHAM5.

4) Circulation: Cyclones and geopotential variations

Transient moisture flux is the transport component due to atmospheric eddies. While the meridional wind component is increasing by height through the troposphere, specific humidity is decreasing. Moisture flux has its highest part in the lower troposphere (Bromwich et al. 1995). The identification of tropospheric wave activity is commonly done at 500 hPa (Blackmon 1976). Owing to the fact that maximum moisture transport occurs in the lower troposphere, 500-hPa wave activity is assumed to be a good measure for the assignment of transient moisture transport to atmospheric circulation. Variations of geopotential height show different characteristics in terms of length scale and temporal frequency. Synoptic-scale variations of the 500-hPa geopotential height field in the frequency band between 2.5 and 8 days represent the storm track (Blackmon 1976) as this band is mainly affected by extratropical cyclones.

Geopotential height variations are analyzed as described in section 2. Figure 4 shows synoptic-scale variations of 500-hPa geopotential height in terms of the square of the anomaly for ERA-40 and ECHAM5. Maximum variations can be found between 50° and 60°S in the Atlantic and Indian Oceans and around 60°S in the Pacific. Decomposition into high- (Fig. 4b) and low-frequency variations (Fig. 4c) highlights different regions. High-frequency variations (i.e., the storm track) show more or less zonal symmetric wave activity with maximum values around 50°S in the Indian Ocean for both reanalysis and the AOGCM. The track density of extratropical cyclones is focused slightly poleward of the storm track, whereas strong cyclone activity corresponds to the maximum of the storm track in the Indian sector of the Southern Ocean (Fig. 5). Strong cyclone-track density of ERA-40 shows another maximum in the Australian sector of the Southern Ocean off the Antarctic coast (Fig. 5b), which is not found in the storm track. The maximum of the low-frequency variation is found around 60°S and southward in the Pacific sector of the Southern Ocean (Figs. 4c,f). Blackmon (1976) discussed NH low-frequency variations of synoptic length scale due to blocking situations that are typically more persistent in comparison to low pressure systems. In the SH, synoptic activity of the Pacific sector of the Southern Ocean is dominated by the Amundsen–Bellingshausen Seas low (ABSL) (e.g., Fogt et al. 2012). This quasi-stationary low steers many cyclones in the direction of West Antarctica (Fogt et al. 2012). The transport of sensible and latent heat is very high in this region (Nicolas and Bromwich 2011). We assume the ABSL to be the reason for the low-frequency variation of the geopotential height field in the Pacific sector of the Southern Ocean.

5) Meridional moisture flux due to different wave frequencies in the twentieth century

A decomposition of the flux into waves of different length scale shows the domination of transport by synoptic-scale waves (Figs. 3c–h) in comparison to

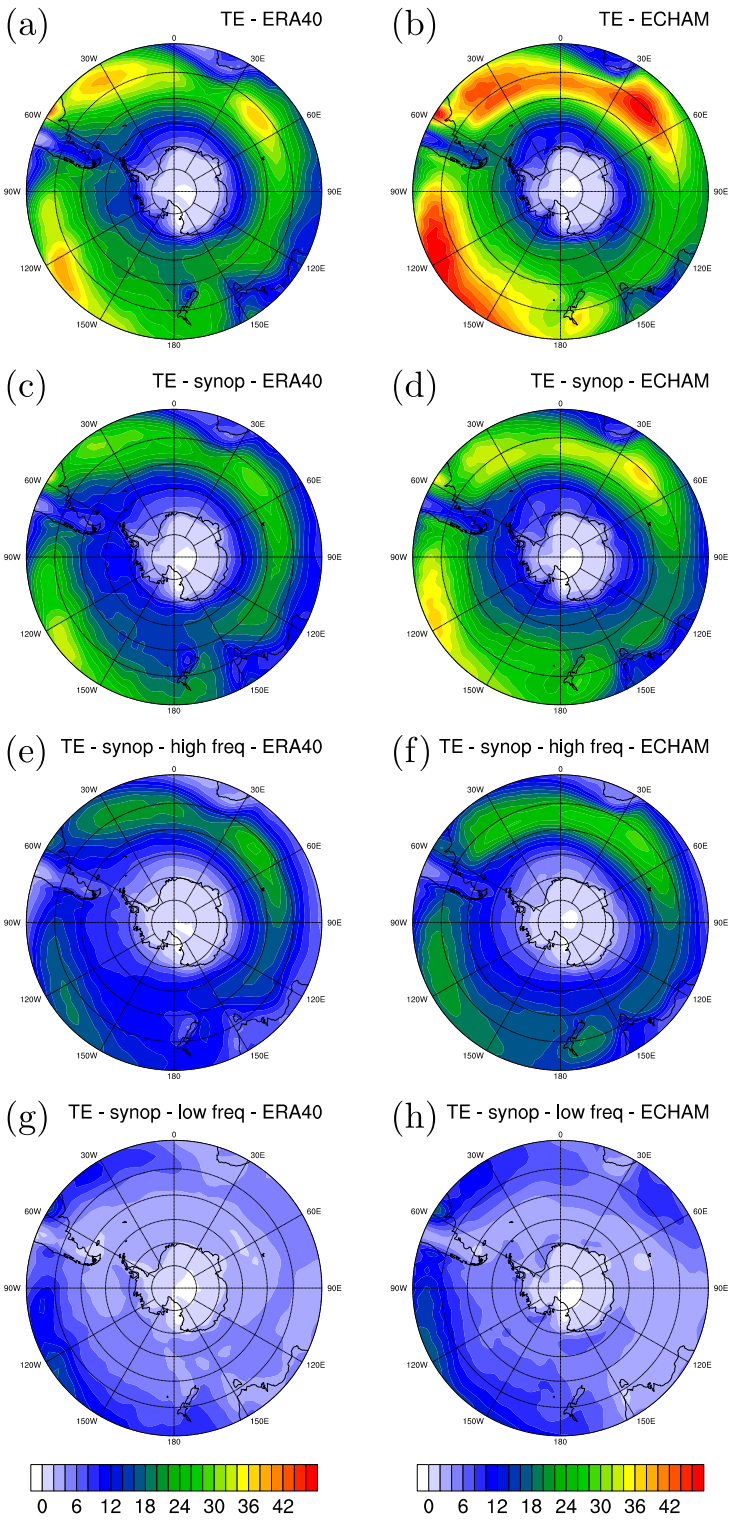

FIG. 3. Transient component of vertically integrated meridional moisture flux ($kg\,m^{-1}\,s^{-1}$) for extended winter season (April–September) between 1981 and 2000 for (a),(c),(e),(g) ERA-40 and (b),(d),(f),(h) ECHAM5 (ensemble of three runs). Flux is (a),(b) not filtered; (c),(d) spatially filtered for synoptic wavelength; and additionally temporal filtered for (e),(f) high and (g),(h) low frequencies.

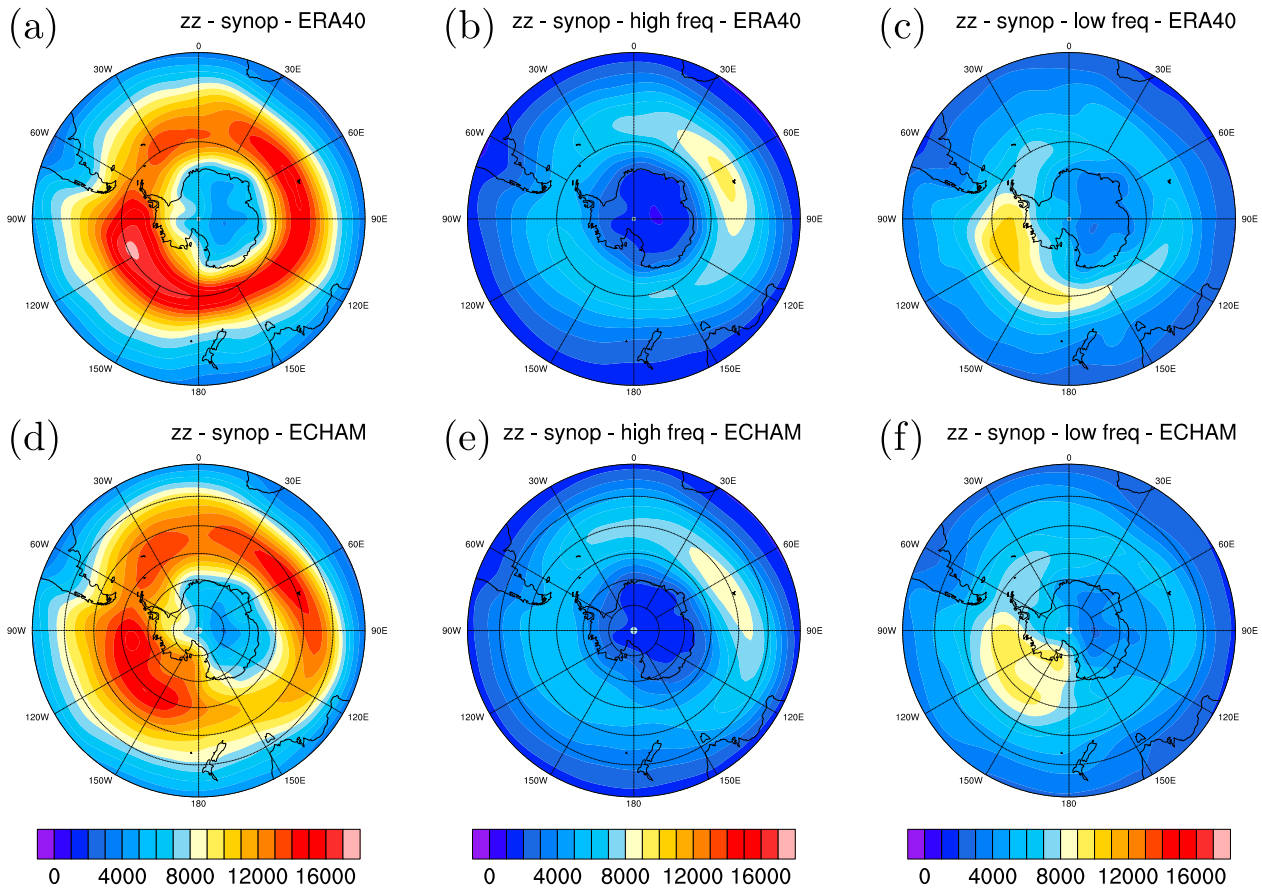

FIG. 4. Variation of the 500-hPa geopotential height anomalies ($z'z'$) (gpm^2) (a),(b),(c) for ERA-40 and (d),(e),(f) simulated by ECHAM5 (ensemble of three runs) for the extended winter season (April–September) between 1981 and 2000 (a),(d) spatially filtered for synoptic wavelength and additionally temporally filtered for (b),(e) high and (c),(f) low frequencies.

transient long waves (not shown). This can also be seen by the comparison of the decomposition with the total flux (Figs. 3a,b). The synoptic-scale waves are split into high- and low-frequency components, as was done for the geopotential height. In the midlatitudes, poleward moisture flux is dominated by the high-frequency component. Maximum values can be found in the Atlantic and Indian sectors of the Southern Ocean. Midlatitude transport due to low-frequency waves is about one order of magnitude smaller in comparison to the high-frequency component. This difference becomes smaller in the high latitudes south of 60°S, where the high-frequency component is, in parts, negligible. South of 60°S, the low-frequency component shows maximum values off the coast of Adelie Land and east of the Ross Sea. In these latitude belts, both components are in the same order of magnitude.

The influence on Antarctica of the different components can be seen for the decomposition of the moisture flux convergence south of 67.5°S (Fig. 6). Total flux is decomposed into the contribution of MMC and TE [Eq. (6)]. Synoptic waves (SW) are part of TE, whereas SW is divided into low- and high-frequency variability. The contributions of the low- and high-frequency components are almost the same.

b. *Simulated changes in the A1B scenario*

1) THERMODYNAMICAL AND DYNAMICAL CHANGE OF MOISTURE FLUX

The AOGCM used in our study shows a distinctive increase of TCWV with respect to the A1B scenario (Fig. 7a), as suggested by previous studies analyzing the model response of the hydrological cycle to temperature changes (Held and Soden 2006). Higher values of TCWV lead to an increasing signal of the meridional moisture flux in the whole analyzed area (Fig. 7b).

Using Eq. (13) allows for the possibility to calculate the dynamical change of moisture flux. This climate change signal of the vertically integrated transient

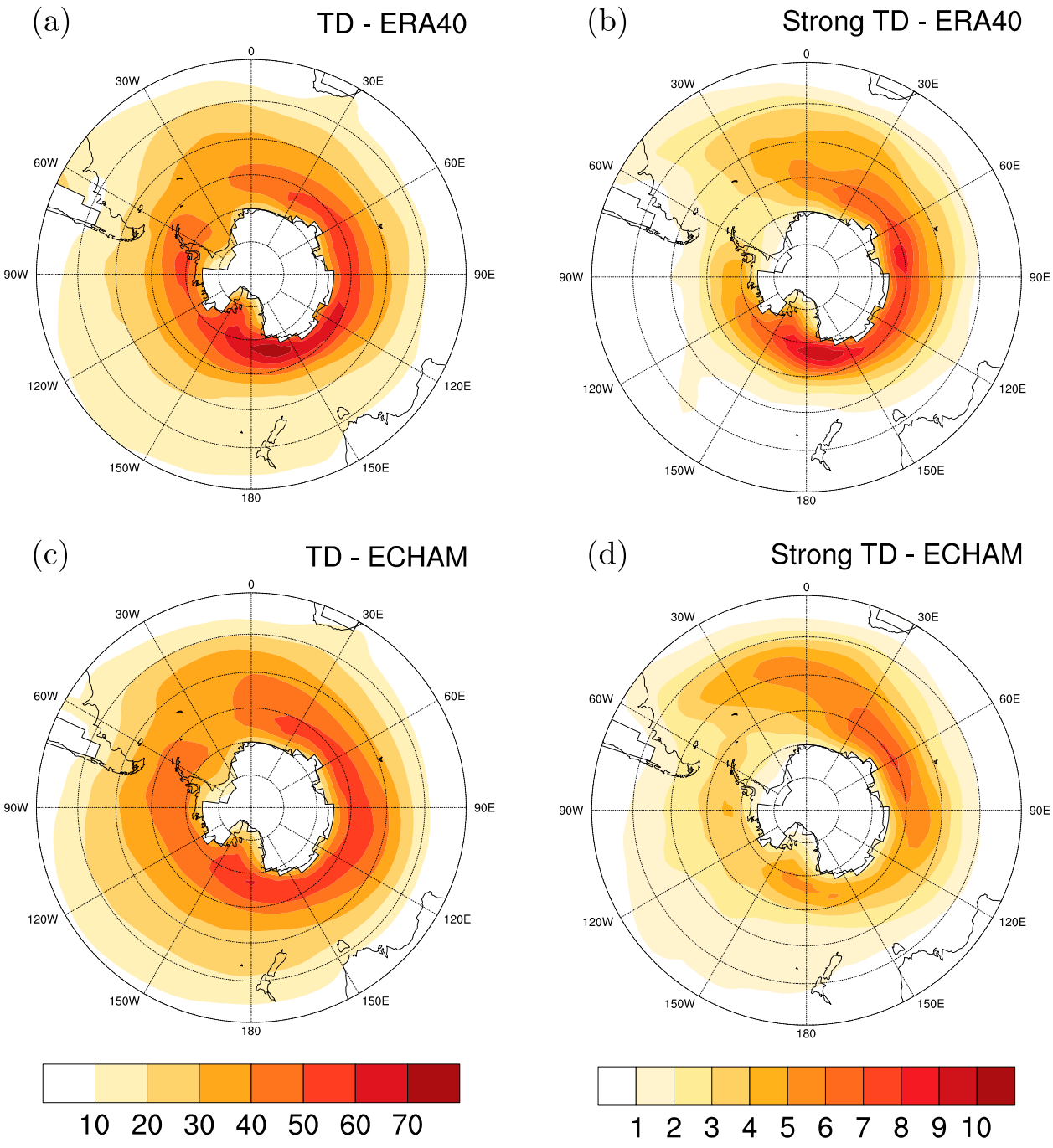

FIG. 5. Cyclone track density [tracks per winter per (degree latitude)^2] identified for (a),(b) ERA-40 and (c),(d) ECHAM5 (ensemble of three runs) for the extended winter season (April–September) between 1981 and 2000 for (a),(c) all and (b),(d) strong cyclones.

moisture flux is dominated by three increasing spots (Fig. 7c), which are found in the Atlantic and the Indian sectors of the Southern Ocean and south of the Tasman Sea. These spots can also be identified in the unscaled total signal as maximum values of the increasing signal (Fig. 7b). In the following, we concentrate on the discussion of the dynamical changes of moisture flux.

2) CHANGES OF DIFFERENT WAVE DECOMPOSITIONS

Because of the small influence of transient long waves on meridional moisture transport, we concentrate on the climate change signals of the synoptic length scale. Figure 8a shows the climate change signal of synoptic

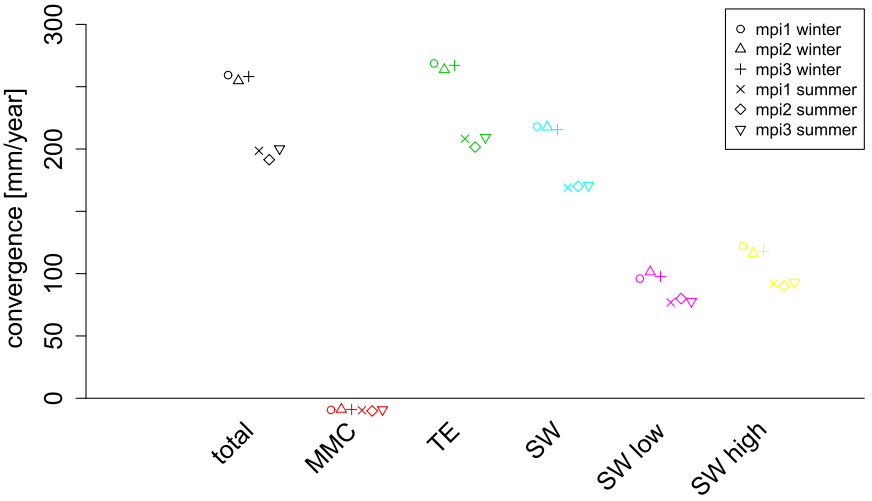

FIG. 6. Moisture flux convergence (mm yr^{-1}) in the twentieth century simulated by three members of ECHAM5 for different temporal and spatial wave activity south of 67.5°S. Summer (October–March) and winter (April–September) are shown separately. The total flux is decomposed into contributions of the MMC and TE. SW are part of TE. SWs are split into low- and high-frequency variations.

length scale variations of the 500-hPa geopotential height field. Wave activity is enhanced in a circumpolar band between 50° and 60°S. This is even more pronounced for the high-frequency component (i.e., the climate change signal of the storm track; Fig. 8b). The intensification of the storm track shows maximum values in the Eastern Atlantic and Indian sectors of the Southern Ocean. Slightly decreasing signals are found north of about 40°S in the Indian and Pacific Oceans. This signal can be interpreted as the commonly named poleward shift of the storm track, which can also be seen in previous studies (e.g., Yin 2005). This characteristic can also be seen in the climate change signal of extratropical cyclones (Fig. 9a) since the storm track is an Eulerian measure for cyclone activity. Low-frequency wave activity shows a decreasing signal over almost the whole SH, but there is a small region of increase in the Pacific Ocean around 45°S and another one south of it. Maximum values of decrease can be seen north and south of the Ross Sea, which is assumed to be a shifted and less variable ABSL. On the other hand, following the discussion of Blackmon (1976), who assigned this low-frequency variability mainly to atmospheric blocking, the decreasing low-frequency variability can be the

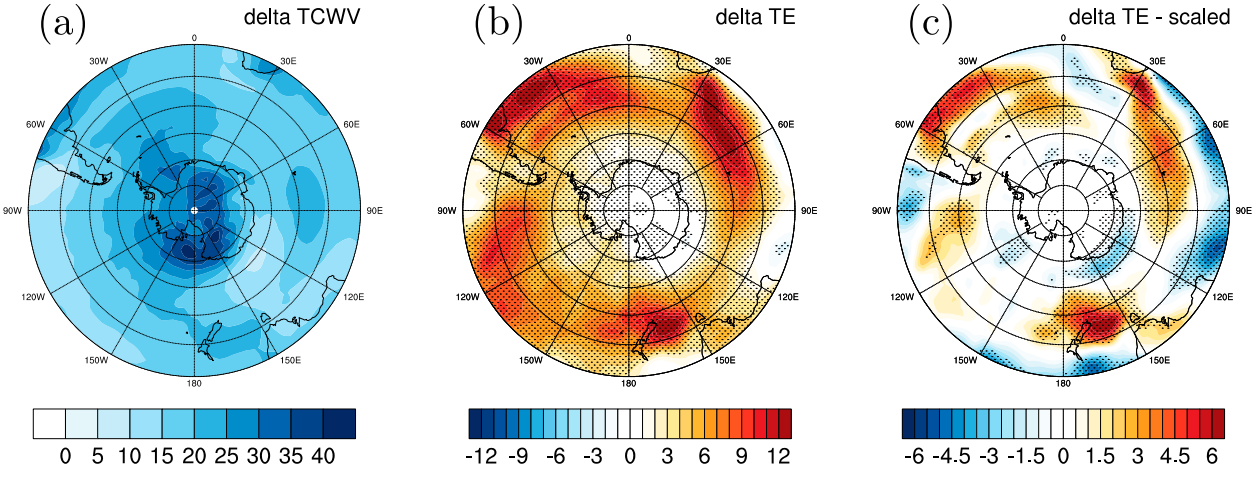

FIG. 7. Climate change signal of (a) TCWV (%), (b) transient meridional moisture flux (kg m^{-1} s^{-1}), and (c) transient meridional moisture flux due to dynamics (kg m^{-1} s^{-1}) . Stippled areas indicate significant changes ($p < 0.05$) with respect to a Students t test. Note that the signal of TCWV is significant everywhere. Therefore, stipples are not shown for TCWV.

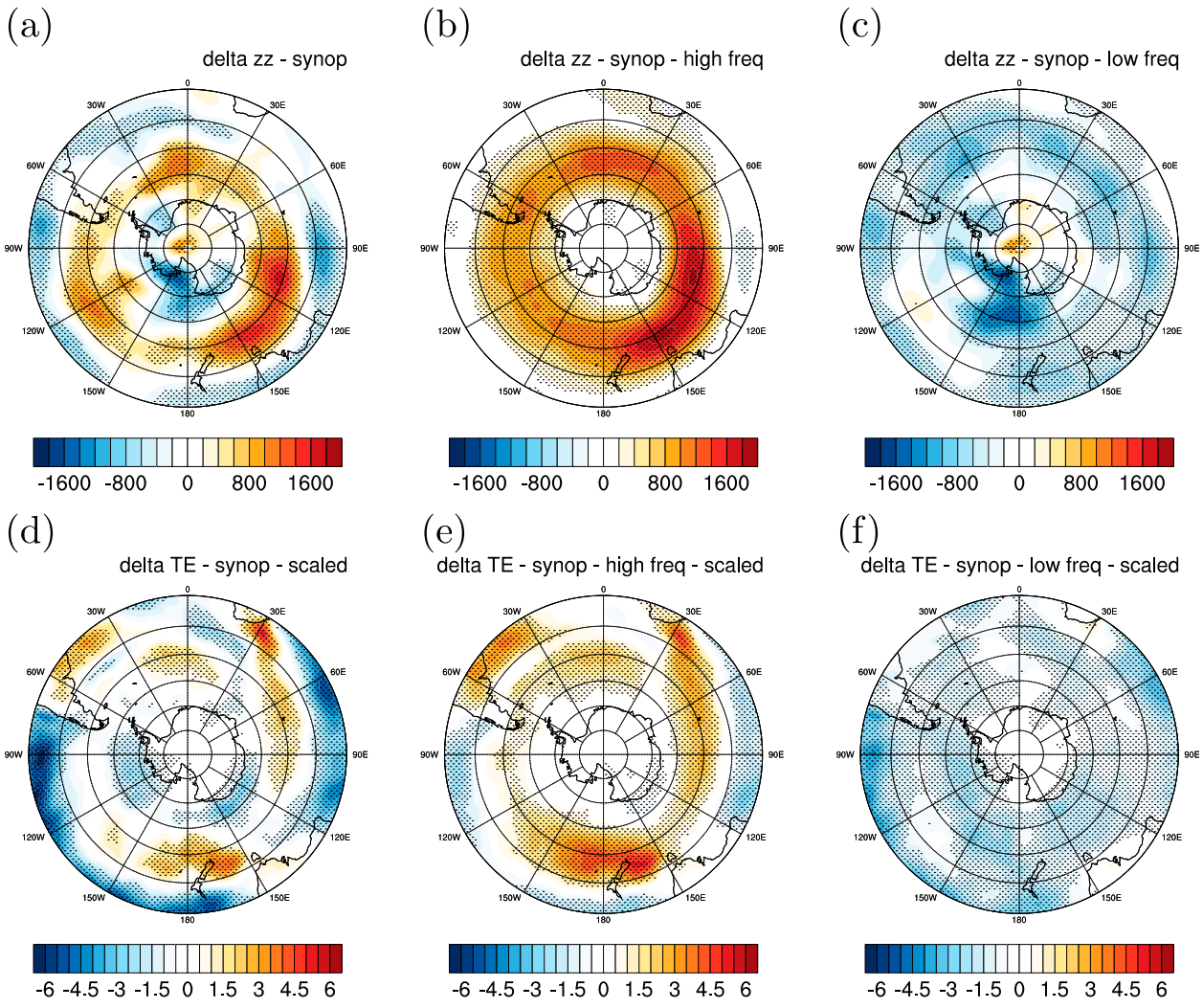

FIG. 8. Climate change signal of synoptic length scale variations of the 500-hPa geopotential height (gpm^2) for (a) all frequencies, (b) high frequencies, and (c) low frequencies; and meridional moisture flux ($kg\,m^{-1}\,s^{-1}$) for (d) all frequencies, (e) high frequencies, and (f) low frequencies. Stippled areas indicate significant changes ($p < 0.05$) with respect to a Students t test.

signal of a future shift toward more frequent situations of low pressure circulation patterns (Lynch et al. 2006).

The dynamical part of the climate change signal of the meridional moisture flux due to synoptic-scale waves shows decreasing poleward flux south of 60°S around Antarctica (Fig. 8d). Increasing poleward flux can be found between 40° and 60°S, whereas a decrease is seen again north of about 40°S mainly in the Indian and Pacific Oceans. The high-frequency component of this signal clearly shows the impact of the shifted storm track (Fig. 8e): that is, an increasing poleward flux between 40° and 60°S and decreases north of it. Besides the shift of the storm track, which can be seen in the change of the variation of the 500-hPa geopotential height (Fig. 8b), maximum values of increases reflect the increasing signal of strong cyclone activity in the South Atlantic, the Eastern Hemisphere, and south of the Tasman Sea (Fig. 9b). The decrease of poleward flux around Antarctica is hardly seen in the high-frequency component. The climate change signal of the low-frequency part shows more or less decreasing poleward flux over the whole SH. Especially the reduction of poleward moisture transport south of 60°S is due to the climate signal of the low-frequency component.

c. *Climate change signal of net precipitation south of the Antarctic Circle*

As previously done in section 3, net precipitation south of a polar spherical cap can be calculated by means of the zonal mean moisture flux at 67.5°S, following Eq. (4). As expected by the climate change signal of meridional moisture flux, which shows increasing poleward

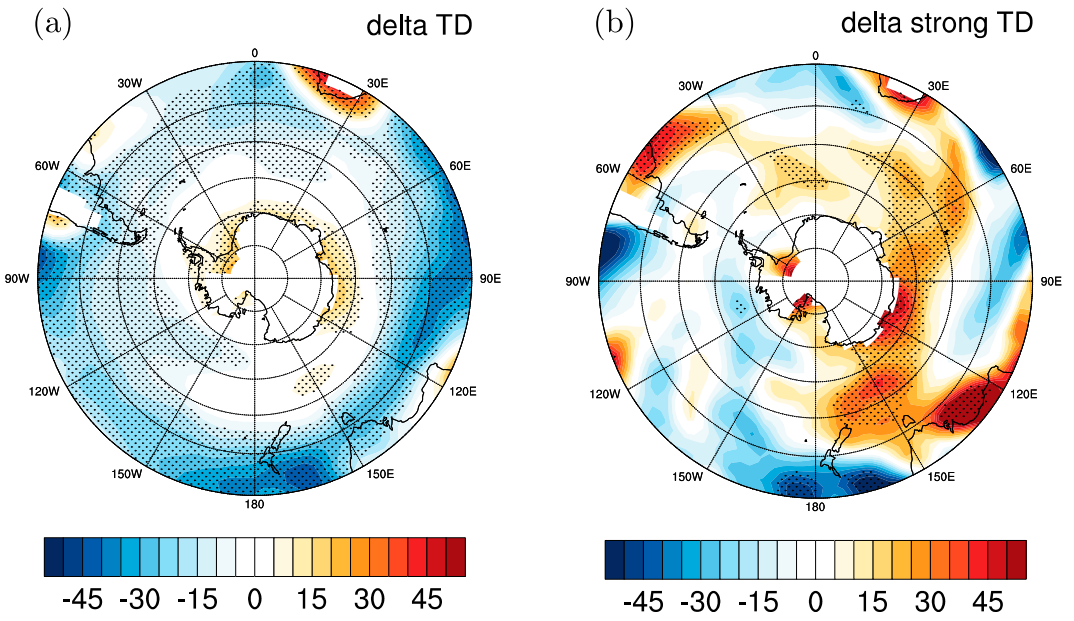

FIG. 9. Relative climate change signal of cyclone-track density (%) for (a) all and (b) strong cyclones. Stippled areas indicate significant changes ($p < 0.05$) with respect to a Students t test.

transports at almost every location of the SH extratropics (Fig. 7b), increasing values for net precipitation can be found south of 67.5°S (Fig. 10a). This is not the case for the dynamical part of the climate signal, which can also be seen for the dynamical signal of the flux (Fig. 7c). For both the twentieth and twenty-first centuries, the synoptic-scale component dominates the whole transient flux divergence within the spherical cap. Dividing this part of the wavelength into low- and high-frequency fluctuations leads to an almost balanced ratio of flux divergence, with 45% for the low-frequency and 55% for the high-frequency component, whereas the low-frequency part of the transient flux in the midlatitudes is an order of magnitude smaller than its high-frequency counterpart (Figs. 3e–h). South of 60°S, the amount of poleward moisture flux is more similar for low and high frequencies, whereas the spatial patterns differ. The high-frequency part shows a zonally symmetric behavior, whereas the main low-frequency flux can be found between the Australian sector of the Southern Ocean (150°E) and the Antarctic Peninsula, where the major moisture inflow toward Antarctica generally takes place.

With respect to the climate change signal, the low-frequency component of the flux divergence shows the highest change of all. This can be seen in the high-latitude climate change signals of moisture flux itself

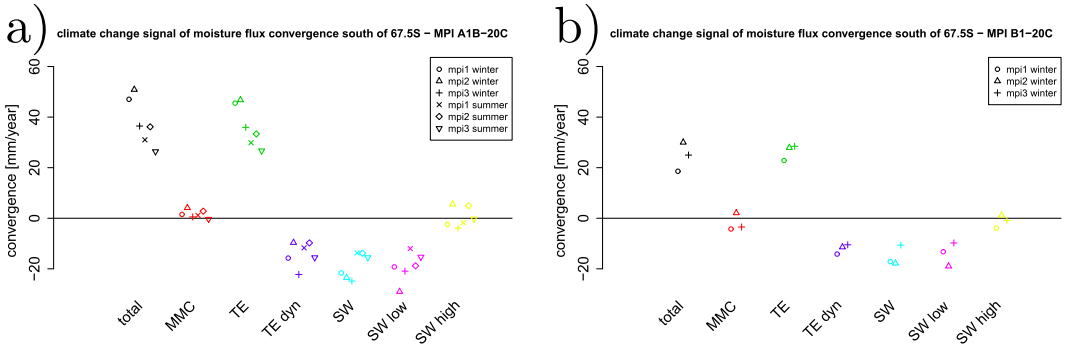

FIG. 10. Climate change signal of the moisture flux convergence (mm yr^{-1}) for (a) the A1B and (b) the B1 scenario simulated by three members of ECHAM5 for different temporal and spatial wave activity south of 67.5°S. In (a), summer (October–March) and winter (April–September) are shown separately. The total flux is decomposed into contributions of the MMC, TE, and the dynamical part of the climate change signal of TE (TE dyn). SW signals are part of TE dyn. SW is split into low- and high-frequency variations.

(Figs. 8e,f). The high-frequency flux component mainly reflects the shift of the SH storm tracks and climate change signal of cyclone activity (Fig. 8e), whereas the signal is negligible at the Antarctic coastline. The low-frequency flux signal is characterized by an opposite sign (i.e., decreasing poleward moisture transport; Fig. 8f), which mainly leads to the decreasing climate change signal of Antarctic net precipitation because of the dynamical component.

Essentially the same results are found for the climate change signal following the B1 scenario. Generally the amplitudes of the signal are less pronounced. The decomposition into different components shows similar behavior as found for the A1B scenario (Figs. 10a,b).

4. Summary, discussion, and conclusions

In this paper, we have analyzed SH moisture flux and net precipitation over Antarctica in the twentieth and twenty-first centuries. For this purpose, reanalysis data and three runs of ECHAM5/MPI-OM integrations were used, both providing 6-hourly output at 11 pressure levels between 1000 and 200 hPa. Furthermore, results were compared with a multimodel ensemble of CMIP5 simulations for daily mean data at one pressure level of 850 hPa. Thermodynamical and dynamical components of the climate signal were distinguished by a scaling approach. While Antarctic net precipitation showed an increase at the end of the twenty-first century, the dynamical component decreased. The dynamical part of the changing signal was analyzed by means of spatial and temporal wave decompositions.

Yin (2005) found a robust poleward shift of the storm track in future projections of a CMIP3 multimodel ensemble. This is consistent with the results of Bengtsson et al. (2006), who investigated cyclone activity in the same model runs analyzed in our study. Also, an examination of a multimodel ensemble that has been investigated in the context of ENSEMBLES (van der Linden and Mitchell 2009) has shown a poleward shift of SH extratropical cyclone-track density as well as an increase of strong cyclones on the Eastern Hemisphere (Grieger et al. 2014). These findings could be reproduced in this paper. Since extratropical cyclones are mainly responsible for mid- and high-latitude transport of atmospheric energy (Peixoto and Oort 1983; Wu et al. 2011), it can be expected that major parts of moisture flux also shift toward the pole. This can be seen in the high-frequency component of the dynamical moisture flux signal, which can be attributed to SH storm track. The climate change signal of this component shows a poleward shift, as seen for the cyclone-track density. Local maxima of the moisture flux signal can be understood by the climate signal of strong extratropical cyclones.

In the SH midlatitudes the low-frequency moisture flux component is an order of magnitude smaller than the high-frequency part. Near the Antarctic coast, the low- and high-frequency moisture fluxes are in the same order of magnitude. Off the coast, quasi-stationary low pressure patterns can be found (cf. Schwerdtfeger 1984), whereas the most prominent is the Amundsen–Bellingshausen Seas Low, also known as Amundsen Sea low (ASL) (Turner et al. 2013). The decrease of the dynamical component of net precipitation is mainly due to the low-frequency variability of moisture flux and is attributed to the ASL. Its characterization and variability is important for synoptic activity (Fogt et al. 2012) as well as the climate of West Antarctica (Hosking et al. 2013). Our analysis seems to uncover ASL fluctuations by means of the low-frequency geopotential height variability. Raphael et al. (2016) analyze the variability of the Amundsen Sea low in CMIP5 models for recent and future climate simulations and find generally deeper mean values for the low with less deep extreme values, which imply less variability of the low. These findings are in line with the finding of our study of decreasing variability in the Amundsen sector (Figs. 8c,f).

Generally, an intensification of atmospheric moisture flux can be identified in future projections of CMIP3 AOGCM simulations (Held and Soden 2006). Obviously, this is considered to be because of an increase of atmospheric moisture in a warmer climate. This can be confirmed by our work, since the model projection shows an overall significant increase of TCWV and an increasing signal of moisture flux due to thermodynamics. This is consistent with the study of Uotila et al. (2007), who find that the thermodynamical part dominates the climate change of SH moisture flux as well as the changes of Antarctic net precipitation. They investigate Antarctic net precipitation for a multimodel ensemble of CMIP3 AOGCMs, which also contains the same ECHAM5 model used in our study. Uotila et al. (2007) have found a good representation of this model in terms of the simulation of Antarctic precipitation. In their study, they criticize the temporal and vertical standard resolution of CMIP3 for an analysis of vertically integrated moisture flux to calculate net precipitation. Therefore, they use model output of precipitation and evaporation for their analysis of Antarctic net precipitation. By means of an investigation of circulation weather types, they distinguish between thermodynamical and dynamical components. In comparison to our results, they do not find a decreasing signal because of dynamics for the whole of Antarctica. For the dynamical component of

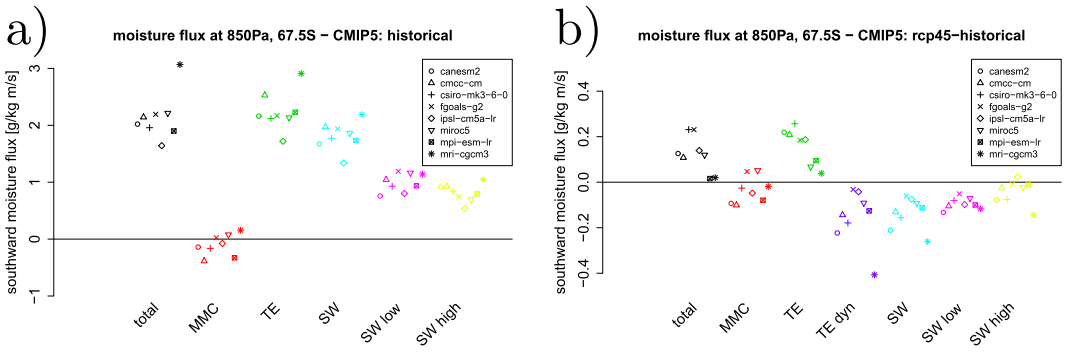

FIG. 11. Components of meridional moisture flux ($g\,kg^{-1}\,m\,s^{-1}$) at 850 hPa and 67.5°S simulated by CMIP5 model runs for (a) the historical forcing and (b) the difference between RCP45 and historical.

the climate change net precipitation, Uotila et al. (2007) found mainly increases for the Antarctic Peninsula and a small decrease for certain parts (i.e., East Antarctica). This different behavior in the dynamical component of the climate change signal reflects the anomalies, which can be found in positive phases of the southern annular mode (SAM), to which climate models tend to shift in future projection (Meehl et al. 2007a). SH Westerlies are then increased and suppress meridional exchange of energy toward East Antarctica, whereas the Antarctic Peninsula is more influenced by flow associated with the mean circulation (van den Broeke and van Lipzig 2004). This characteristic is potentially less pronounced in our study since it concentrates on transient transports of moisture, whereas the direct impact of SAM as described above is more characterized in the mean meridional circulation. Furthermore, Uotila et al. (2007) used precipitation and evaporation, where AOGCMs potentially still have problems dealing with the Antarctic region (cf. Genthon and Krinner 2001).

At the end of the twenty-first century of the warm A1B scenario, it is expected that Antarctic sea ice will decrease. Bader et al. (2013) show sea ice reduction for the same ECHAM5 model for simulations following the A1B scenario (their Fig. 1a). They analyze the atmospheric response on this sea ice reduction and find an equatorward shift of cyclone-track density as well as precipitation patterns. On the other hand, the largest precipitation response is detected in regions where sea ice reduction is large and thus vertical increases of ocean–atmosphere heat flux is found. Our study implicitly takes into account both phenomena. Increasing amount of moisture content is attributed to the thermodynamical signal, whereas the change of the circulation pattern is part of the dynamical climate change signal.

In our study, net precipitation in terms of moisture flux convergence is calculated separately for each ECHAM5 ensemble member. Results for the twentieth century are very similar (Fig. 6), whereas the members show some spread for the climate change signals (Fig. 10). In the twentieth century, it is easy to distinguish between the summer and winter seasons, whereas the climate change signal is very similar for the seasons.

We investigated further robustness of our results of net precipitation change by means of a CMIP5 multimodel ensemble (Fig. 11). Because of data availability, the comparison is done for one single pressure level (i.e., 850 hPa), where moisture flux seems to be maximal near the Antarctic coast (Bromwich et al. 1995). The different flux components of the CMIP5 models for the historical simulation show a behavior that is comparable with our results of the ECHAM5 runs (Figs. 6 and 10). Also, the finding of moisture flux increase in the projection and the decrease of the dynamical component mainly due to the low-frequency component can be reproduced by the CMIP5 ensemble. The spread of the CMIP5 model results is not investigated in our study and is worthwhile to analyze in further research.

Acknowledgments. This work was supported by the SACAI project (LE 1865/1-1), funded by the DFG Priority Programme 1158 "Antarctic Research." We thank ECMWF for ERA-40 data use and availability. We acknowledge the World Climate Research Programme's Working Group on Coupled Modelling, which is responsible for CMIP, and we thank the climate modeling groups (listed in Table 1 of this paper) for producing and making available their model output. For CMIP, the U.S. Department of Energy's Program for Climate Model Diagnosis and Intercomparison provides coordinating support and led development of software infrastructure in partnership with the Global Organization for Earth System Science Portals. We are grateful to Kevin Keay (School of Earth Sciences, University of Melbourne) for his language revisions to the manuscript.

Many thanks to the anonymous reviewers for their work and constructive comments.

REFERENCES

Bader, J., M. Flgge, N. Kvamst, M. Mesquita, and A. Voigt, 2013: Atmospheric winter response to a projected future Antarctic sea-ice reduction: A dynamical analysis. *Climate Dyn.*, **40**, 2707–2718, doi:10.1007/s00382-012-1507-9.

Bengtsson, L., K. I. Hodges, and E. Roeckner, 2006: Storm tracks and climate change. *J. Climate*, **19**, 3518–3543, doi:10.1175/JCLI3815.1.

Blackmon, M. L., 1976: A climatological spectral study of 500-mb geopotential height of Northern Hemisphere. *J. Atmos. Sci.*, **33**, 1607–1623, doi:10.1175/1520-0469(1976)033<1607:ACSSOT>2.0.CO;2.

Bromwich, D. H., 1988: Snowfall in high southern latitudes. *Rev. Geophys.*, **26**, 149–168, doi:10.1029/RG026i001p00149.

——, and F. M. Robasky, 1993: Recent precipitation trends over the polar ice sheets. *Meteor. Atmos. Phys.*, **51**, 259–274, doi:10.1007/BF01030498.

——, and R. L. Fogt, 2004: Strong trends in the skill of the ERA-40 and NCEP–NCAR reanalyses in the high and midlatitudes of the Southern Hemisphere, 1958–2001. *J. Climate*, **17**, 4603–4619, doi:10.1175/3241.1.

——, F. M. Robasky, R. I. Cullather, and M. L. Vanwoert, 1995: The atmospheric hydrologic cycle over the Southern Ocean and Antarctica from operational numerical analyses. *Mon. Wea. Rev.*, **123**, 3518–3538, doi:10.1175/1520-0493(1995)123<3518:TAHCOT>2.0.CO;2.

——, Z. C. Guo, L. S. Bai, and Q. S. Chen, 2004: Modeled Antarctic precipitation. Part I: Spatial and temporal variability. *J. Climate*, **17**, 427–447, doi:10.1175/1520-0442(2004)017<0427:MAPPIS>2.0.CO;2.

Church, J., and Coauthors, 2013: Sea level change. *Climate Change 2013: The Physical Science Basis*, T. F. Stocker et al., Eds., Cambridge University Press, 1137–1216, doi:10.1017/CBO9781107415324.026.

Connolley, W. M., and J. C. King, 1993: Atmospheric water-vapor transport to Antarctica inferred from radiosonde data. *Quart. J. Roy. Meteor. Soc.*, **119**, 325–342, doi:10.1002/qj.49711951006.

Cullather, R. I., D. H. Bromwich, and M. L. Van Woert, 1998: Spatial and temporal variability of Antarctic precipitation from atmospheric methods. *J. Climate*, **11**, 334–367, doi:10.1175/1520-0442(1998)011<0334:SATVOA>2.0.CO;2.

Fogt, R. L., A. J. Wovrosh, R. A. Langen, and I. Simmonds, 2012: The characteristic variability and connection to the underlying synoptic activity of the Amundsen–Bellingshausen Seas Low. *J. Geophys. Res.*, **117**, D07111, doi:10.1029/2011JD017337.

Frieler, K., and Coauthors, 2015: Consistent evidence of increasing Antarctic accumulation with warming. *Nat. Climate Change*, **5**, 348–352, doi:10.1038/nclimate2574.

Genthon, C., and G. Krinner, 2001: Antarctic surface mass balance and systematic biases in general circulation models. *J. Geophys. Res.*, **106**, 20 653–20 664, doi:10.1029/2001JD900136.

Grieger, J., G. Leckebusch, M. Donat, M. Schuster, and U. Ulbrich, 2014: Southern Hemisphere winter cyclone activity under recent and future climate conditions in multi-model AOGCM simulations. *Int. J. Climatol.*, **34**, 3400–3416, doi:10.1002/joc.3917.

Held, I. M., and B. J. Soden, 2006: Robust responses of the hydrological cycle to global warming. *J. Climate*, **19**, 5686–5699, doi:10.1175/JCLI3990.1.

Hosking, J. S., A. Orr, G. J. Marshall, J. Turner, and T. Phillips, 2013: The influence of the Amundsen–Bellingshausen Seas Low on the climate of West Antarctica and its representation in coupled climate model simulations. *J. Climate*, **26**, 6633–6648, doi:10.1175/JCLI-D-12-00813.1.

Lorenz, D. J., and E. T. DeWeaver, 2007: The response of the extratropical hydrological cycle to global warming. *J. Climate*, **20**, 3470–3484, doi:10.1175/JCLI4192.1.

Lynch, A., P. Uotila, and J. J. Cassano, 2006: Changes in synoptic weather patterns in the polar regions in the twentieth and twenty-first centuries. Part 2: Antarctic. *Int. J. Climatol.*, **26**, 1181–1199, doi:10.1002/joc.1305.

Marsland, S., H. Haak, J. Jungclaus, M. Latif, and F. Röske, 2003: The Max-Planck-Institute global ocean/sea ice model with orthogonal curvilinear coordinates. *Ocean Modell.*, **5**, 91–127, doi:10.1016/S1463-5003(02)00015-X.

Meehl, G. A., and Coauthors, 2007a: Global climate projections. *Climate Change 2007: The Physical Science Basis*, S. Solomon et al., Eds., Cambridge University Press, 747–846.

——, C. Covey, T. Delworth, M. Latif, B. McAvaney, J. F. B. Mitchell, R. J. Stouffer, and K. E. Taylor, 2007b: The WCRP CMIP3 multimodel dataset: A new era in climate change research. *Bull. Amer. Meteor. Soc.*, **88**, 1383–1394, doi:10.1175/BAMS-88-9-1383.

Monaghan, A. J., D. H. Bromwich, and S. H. Wang, 2006: Recent trends in Antarctic snow accumulation from Polar MM5 simulations. *Philos. Trans. Roy. Soc.*, **A364**, 1683–1708, doi:10.1098/rsta.2006.1795.

Murray, R., and I. Simmonds, 1991: A numerical scheme for tracking cyclone centres from digital data. Part I: Development and operation of the scheme. *Aust. Meteor. Mag.*, **39**, 155–166.

Nakicenovic, N., and Coauthors, 2000: *Special Report on Emissions Scenarios*. Cambridge University Press, 599 pp.

Nicolas, J. P., and D. H. Bromwich, 2011: Climate of West Antarctica and influence of marine air intrusions. *J. Climate*, **24**, 49–67, doi:10.1175/2010JCLI3522.1.

Peixoto, J. P., and A. H. Oort, 1983: The atmospheric branch of the hydrological cycle and climate. *Variations in the Global Water Budget*, A. Street-Perrott, M. Beran, and R. Ratcliffe, Eds., Reidel, 5–65.

——, and ——, 1992: *Physics of Climate.* Springer, 520 pp.

Raphael, M. N., and Coauthors, 2016: The Amundsen Sea Low: Variability, change, and impact on Antarctic climate. *Bull. Amer. Meteor. Soc.*, doi:10.1175/BAMS-D-14-00018.1, in press.

Roeckner, E., and Coauthors, 2003: The atmospheric general circulation model ECHAM 5. Part I: Model description. Max Planck Institute for Meteorology Tech. Rep. 349, 127 pp. [Available online at https://www.mpimet.mpg.de/fileadmin/publikationen/Reports/max_scirep_349.pdf.]

Schwerdtfeger, W., 1984: *Weather and Climate of the Antarctic.* Elsevier Science, 261 pp.

Seager, R., N. Naik, and G. A. Vecchi, 2010: Thermodynamic and dynamic mechanisms for large-scale changes in the hydrological cycle in response to global warming. *J. Climate*, **23**, 4651–4668, doi:10.1175/2010JCLI3655.1.

Simmonds, I., and R. J. Murray, 1999: Southern extratropical cyclone behavior in ECMWF analyses during the frost special observing periods. *Wea. Forecasting*, **14**, 878–891, doi:10.1175/1520-0434(1999)014<0878:SECBIE>2.0.CO;2.

——, ——, and R. M. Leighton, 1999: A refinement of cyclone tracking methods with data from frost. *Aust. Meteor. Mag.*, **1999**, 35–49.

Taylor, K. E., R. J. Stouffer, and G. A. Meehl, 2012: An overview of CMIP5 and the experiment design. Bull. *Amer. Meteor. Soc.*, **93**, 485–498, doi:10.1175/BAMS-D-11-00094.1.

Tietvinen, H., and T. Vihma, 2008: Atmospheric moisture budget over Antarctica and the Southern Ocean based on the ERA-40 reanalysis. *Int. J. Climatol.*, **28**, 1977–1995, doi:10.1002/joc.1684.

Turner, J., T. A. Lachlan-Cope, J. P. Thomas, and S. R. Colwell, 1995: The synoptic origins of precipitation over the Antarctic Peninsula. *Antarct. Sci.*, **7**, 327–337, doi:10.1017/S0954102095000447.

——, and Coauthors, Eds., 2009: *Antarctic Climate Change and the Environment*. Scientific Committee on Antarctic Research, 526 pp.

——, T. Phillips, J. S. Hosking, G. J. Marshall, and A. Orr, 2013: The Amundsen Sea low. *Int. J. Climatol.*, **33**, 1818–1829, doi:10.1002/joc.3558.

Uotila, P., A. H. Lynch, J. J. Cassano, and R. I. Cullather, 2007: Changes in Antarctic net precipitation in the 21st century based on Intergovernmental Panel on Climate Change (IPCC) model scenarios. *J. Geophys. Res.*, **112**, D10107, doi:10.1029/2006JD007482.

Uppala, S. M., and Coauthors, 2005: The ERA-40 Re-Analysis. *Quart. J. Roy. Meteor. Soc.*, **131**, 2961–3012, doi:10.1256/qj.04.176.

van den Broeke, M. R., and N. P. M. van Lipzig, 2004: Changes in Antarctic temperature, wind and precipitation in response to the Antarctic Oscillation. *Ann. Glaciol.*, **39**, 119–126, doi:10.3189/172756404781814654.

van der Linden, P., and J. Mitchell, 2009: *ENSEMBLES: Climate Change and Its Impacts: Summary of Research and Results from the ENSEMBLES Project*. Met Office Hadley Centre, 160 pp.

Wu, Y. T., M. F. Ting, R. Seager, H. P. Huang, and M. A. Cane, 2011: Changes in storm tracks and energy transports in a warmer climate simulated by the GFDL CM2.1 model. *Climate Dyn.*, **37**, 53–72, doi:10.1007/s00382-010-0776-4.

Yamazaki, K., 1992: Moisture budget in the Antarctic atmosphere. *Proc. NIPR Symp. Polar Meteor. Glaciol.*, **6**, 36–45. [Available online at http://ci.nii.ac.jp/naid/110001025932/en.]

Yin, J. H., 2005: A consistent poleward shift of the storm tracks in simulations of 21st century climate. *Geophys. Res. Lett.*, **32**, L18701, doi:10.1029/2005GL023684.